

*Chapter 3***Electrocatalytic Ammonia Oxidation Mediated by a Polypyridyl Iron Catalyst**

Adapted from:

Zott, M. D.;[‡] Garrido-Barros, P.;[‡] Peters, J. C.

ACS Catal. **2019**, *9*, 10101–10108.

DOI: 10.1021/acscatal.9b03499

3.1 Introduction

Ammonia is produced on a massive scale globally by industrial nitrogen fixation, primarily for use as fertilizer. New ammonia synthesis technologies may yet enable other vectors for ammonia use, for example as a transportation fuel. Accordingly, there are substantial efforts underway to explore whether electrocatalytic N₂-to-NH₃ (N₂RR) conversion, potentially coupled with renewable resources that generate electricity, could provide a new ammonia synthesis pathway (Equation 3.1) to be exploited in renewably formed fuel storage, transport, and on-site use.¹



Commensurate with these goals, there has been long-standing interest in exploring heterogeneous catalysts for selective ammonia oxidation (AO), the microscopic reverse of N₂-to-NH₃ conversion (Equation 3.1).² The realization of selective electrocatalysts for AO in principle could enable fuel cell applications for ammonia, akin to those currently being practiced or explored for hydrogen and methanol.³

Homogeneous (electro)catalysts for N₂RR and AO have much to offer in terms of fundamental mechanistic studies, and possibly longer-term practical applications if robust hybrid catalyst/electrode architectures can be realized. Indeed, the field of N₂RR catalysis mediated by molecular systems has witnessed a surge of activity in the past 10–15 years, in part motivated by a desire to explore hypotheses germane to the inorganic mechanism of biological nitrogen fixation.⁴ This has been matched by significant progress in defining catalysts (e.g., featuring Mo or Fe) that operate with (comparatively) impressive turnovers

and selectivities, and in fundamental mechanistic understanding of how these transformations occur.⁵ Interest in translating this progress to electrocatalytic N₂RR using synthetic coordination complexes is growing.⁶

By contrast, homogeneous approaches to ammonia oxidation have been slower to attract significant attention from the coordination chemistry community. This is surprising given that biological ammonia oxidation, mediated by both aerobic and anaerobic ammonia-oxidizing bacteria, involves steps thought to occur at iron, copper, or molybdenum active sites, and is essential to the global nitrogen cycle.⁷ As a six-electron process with substantial kinetic barriers, this process presents fascinating challenges in energy conversion, electrochemistry, and coordination chemistry. Challenges associated with catalytically converting NH₃ to N₂ and proton/electron equivalents at a well-defined active site include the fact that NH₃ is a strong σ -donor ligand that features thermally robust N–H bonds (BDFE_{N–H} = 99.4 kcal/mol).⁸

Despite the comparatively limited activity in this area, stoichiometric oxidation of ammonia is well preceded. For instance, in 1979 Buhr and Taube initiated the study of ammonia oxidation by molecular complexes when they reported both chemical and electrochemical oxidation of ammonia in aqueous solution by [Os(NH₃)₅(CO)]²⁺ to form N₂ in the μ -N₂-bridged product [(Os(NH₃)₄(CO))₂N₂]⁴⁺ (Chart 3.1, A).⁹ Relatedly, Thompson and Meyer reported the stoichiometric electrochemical oxidation of ammonia to nitrite and nitrate by [(trpy)(bpy)Ru(NH₃)]²⁺ (trpy = 2,2':6',2''-terpyridine, bpy = 2,2'-bipyridine) in aqueous solution (Chart 3.1, B),¹⁰ and reported electrochemical (though not electrocatalytic) ammonia oxidation to N₂ by a similar ruthenium polypyridyl system,

$[(bpy)_2(NH_3)RuORu(NH_3)(bpy)_2]^{4+}$.¹¹ Collman and coworkers have studied chemical and electrochemical oxidation of ammonia at cofacial ruthenium porphyrins via hydrazine and diazene intermediates.¹² Most recently, Hamann, Smith, and coworkers demonstrated that modification of the Meyer system provides a bona fide electrocatalyst for ammonia oxidation to N_2 , reporting the liberation of 2.1 eq N_2 at 0.2 V vs Fc/Fc^+ (0.03 V onset potential) under the conditions used (Chart 3.1, C).¹³

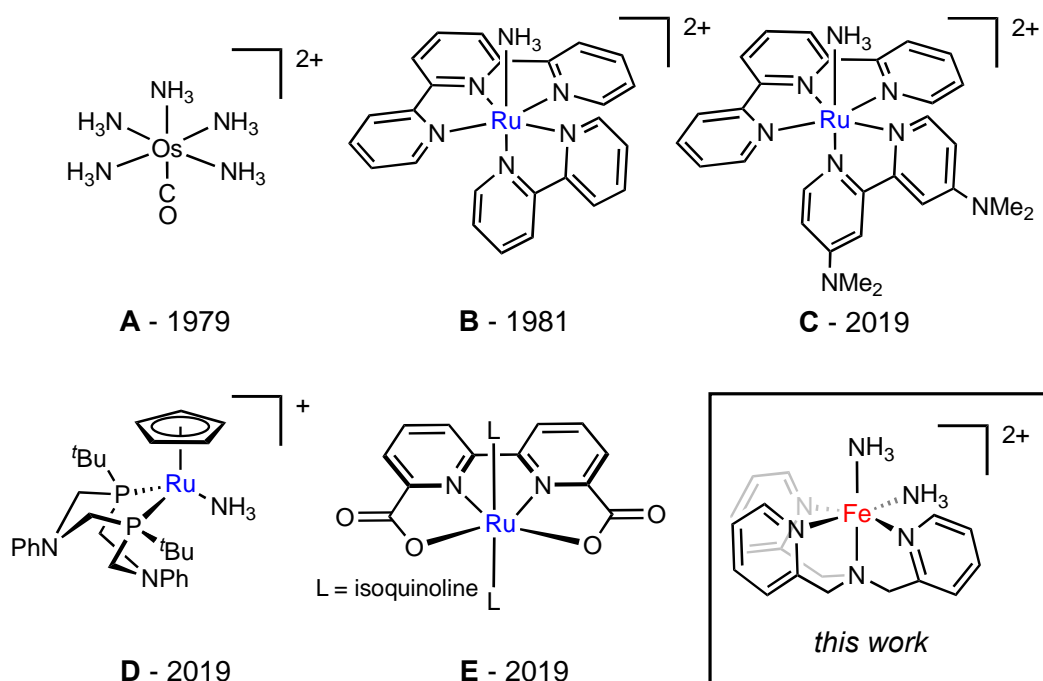


Chart 3.1. Molecular complexes that mediate AO.

There has also been growing interest in exploring molecular catalysts for ammonia oxidation that operate via net H-atom abstraction chemistry. In this context, a number of fascinating recent reports describe H-atom abstraction (HAA) reactions from coordinated NH_3 , which can lead to $M(NH_2)$, $M(NH)$, $M(N)$, and in certain cases N_2 (via nitride coupling).¹⁴ Catalytic ammonia oxidation via HAA has also been recently demonstrated using a ruthenium complex and 2,4,6-tri(*t*-butyl)phenoxy radical by Mock and coworkers

(Chart 3.1, D).¹⁵ Similarly, Nishibayashi and coworkers recently reported catalytic chemical oxidation of ammonia, again using a ruthenium system (Chart 3.1, E).¹⁶

Given the paucity of data available describing electrocatalytic ammonia oxidation, and the fact that biologically relevant first row metals such as iron have yet to be described for this process, we targeted the study of promising candidate iron (electro)catalysts as models well-suited to mechanistic interrogation. Noting that a number of polypyridyl iron complexes have been studied as potential water oxidation catalysts (WOC's),¹⁷ we felt such systems might provide a prudent starting point.

In this context, we now describe that a previously reported iron complex featuring a tetradentate polypyridyl supporting ligand (TPA) and two cis-labile sites, $[(\text{TPA})\text{Fe}(\text{MeCN})_2]^{2+}$,¹⁸ is highly active for electrocatalytic ammonia oxidation in acetonitrile under an applied bias. Important features of this system are that NH_3 can reversibly bind at the two labile sites, NH_3 itself is able to promote the proton-transfer steps needed for catalytic activity, and up to 16 eq of N_2 (per Fe) have been generated from NH_3 using this catalyst via controlled potential coulometry (CPC) experiments. At present, this is the highest TON to be verified for a molecular AO system. More importantly, the system is electrochemically well behaved and hence amenable to detailed study by a range of electrochemical experiments. Our data point to an observed rate constant, k_{obs} , for NH_3 oxidation of $\sim 10^7 \text{ M}^{-1} \cdot \text{s}^{-1}$, with the catalytic process starting at an onset potential of $\sim 0.7 \text{ V}$ vs Fc/Fc^+ , whose rate-determining step (RDS) is first order in $[(\text{TPA})\text{Fe}(\text{L})_2]^{2+}$ and NH_3 . The available data also allow us to suggest $[(\text{TPA})\text{Fe}^{\text{III}}(\text{NH}_2)(\text{NH}_3)]^{2+}$ and $[(\text{TPA})\text{Fe}^{\text{IV}}(\text{NH}_2)(\text{NH}_3)]^{3+}$ species as early intermediates en route to N–N bond formation.

3.2 Results and Discussion

3.2.1 Electrocatalytic conversion of NH₃ to N₂ and H₂. The cyclic voltammogram of [(TPA)Fe(MeCN)₂]OTf₂ in acetonitrile using a boron-doped diamond (BDD) working electrode (see Figure 3.1A,B) has one reversible feature at 0.75 V vs Fc/Fc⁺ corresponding to the Fe²⁺/Fe³⁺ redox couple (Figure 3.1A). Two new redox features appeared (*E*₁ and *E*₂) in the presence of increasing amounts of added NH₃, and the reversible feature corresponding to [(TPA)Fe(MeCN)₂]OTf₂ disappeared. Moreover, the wave at *E*₂ continuously increased with increasing ammonia concentration. As a reference, when 100 equivalents of NH₃ were added to the [(TPA)Fe(MeCN)₂]OTf₂ solution in acetonitrile, *E*₁ and *E*₂ were centered at 0.4 V and 1.1 V, respectively, and *E*₂ featured dramatically increased current relative to that

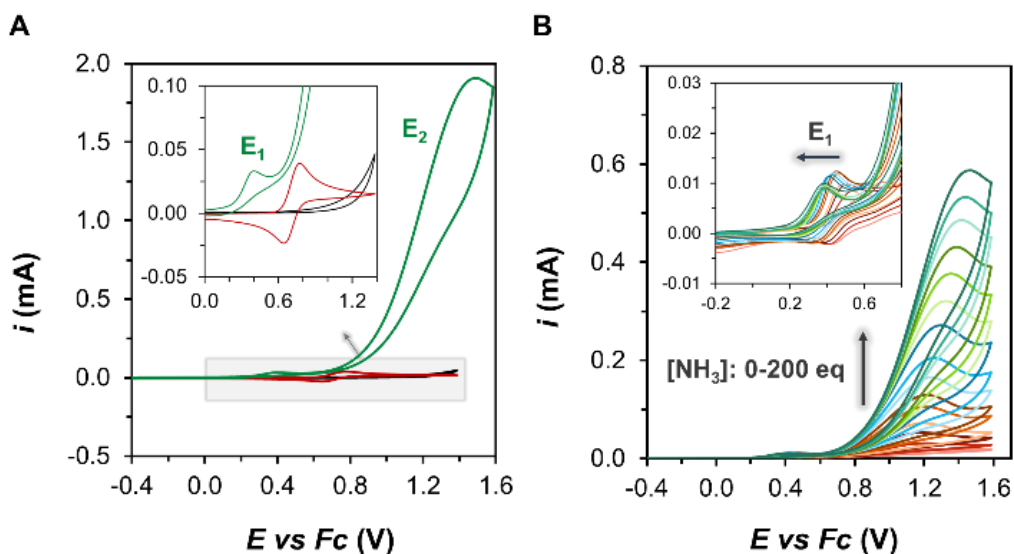


Figure 3.1. Electrochemical data. (A) Cyclic voltammograms in acetonitrile solutions of background AO on BDD in presence of 0.25 M NH₃ (black), 2.5 mM [(TPA)Fe(MeCN)₂]OTf₂ in the absence of NH₃ (red), and AO by [(TPA)Fe(MeCN)₂]OTf₂ with 0.25 M NH₃ (green). (B) Cyclic voltammograms in acetonitrile with 50 mM NH₄OTf and 0.5 mM [(TPA)Fe(MeCN)₂]OTf₂ with varying [NH₃]. The inset highlights the shift in *E*₁ with [NH₃]. CVs were recorded with a BDD disk electrode, a Pt counter electrode, and a custom Ag/AgOTf reference electrode corrected for the Fc/Fc⁺ couple.

observed for the one-electron $\text{Fe}^{2+}/\text{Fe}^{3+}$ redox couple. These observations are consistent with fast electrocatalytic ammonia oxidation at E_2 .

To assess whether catalytic NH_3 oxidation occurs at the irreversible E_2 wave, CPC was performed using a BDD plate working electrode (1 cm^2) and a Pt counter electrode to facilitate H_2 evolution, and the headspace was analyzed via gas chromatography. CPC of a $0.5 \text{ mM } [(\text{TPA})\text{Fe}(\text{MeCN})_2]\text{OTf}_2$ acetonitrile solution with $65 \text{ mM } \text{NH}_3$ was performed at 1.1 V vs Fc/Fc^+ . After 18 h, 33 C of charge had passed; headspace analysis indicated Faradaic efficiencies of 80% and 70% for the production of N_2 and H_2 ($\pm 10\%$ error in gas quantification), respectively, correlating with the production of up to 16 equivalents of N_2 .¹⁹ This turnover number is the highest yet reported for a molecular NH_3 oxidation (electro)catalyst. The measured $\text{H}_2:\text{N}_2$ ratio was 2.6:1, in good agreement with the 3:1 ratio expected for NH_3 . When isotopically enriched $^{15}\text{NH}_4\text{OTf}$ and $^{15}\text{NH}_3$ were employed, only $^{30}\text{N}_2$ was observed by GC-MS, confirming ammonia to be the source of detected N_2 (see SI for details).

Further CPC experiments in the absence of a (TPA)Fe source, at the same applied potential of 1.1 V vs Fc/Fc^+ , suggest a critical role for (TPA)Fe-species in the catalysis. When CPC of a $65 \text{ mM } \text{NH}_3$ solution was performed, only 1.1 C of charge was passed, and only 0.5 eq N_2 were detected. Furthermore, when $[(\text{TPA})\text{Fe}(\text{MeCN})_2]\text{OTf}_2$ was replaced with FeOTf_2 as the precatalyst, only 1.9 C of charge were passed along with 1.0 eq N_2 being detected in the headspace.

3.2.2 Investigation of catalyst stability. Over multiple independent CPC experiments, the current after 18 h at an applied potential of 1.1 V vs Fc/Fc^+ had greatly attenuated. Such a

decrease in current typically suggests either catalyst decomposition or electrode passivation.²⁰ To study this phenomenon, X-ray photoelectron spectroscopy was performed on the BDD working electrode after CPC to try to identify potential degradation products. During CPC with 65 mM NH₃ and no added iron precatalyst, the current dropped to 10% of the initial current after only 3 h. XPS analysis of the BDD electrode revealed incorporation of nitrogen onto the electrode surface (see SI). This process passivates the electrode surface, as confirmed by measurements of the ferrocene/ferrocenium redox couple before and after CPC. This passivation is hence one process by which the catalysis can be arrested in the presence of NH₃ using BDD electrodes.

Although the chronoamperogram with [(TPA)Fe(MeCN)₂]OTf₂ as a precatalyst in the presence of NH₃ also showed a time-dependent decrease in current, a much longer time scale, ~15 h, was required to reach 10% of the initial current. Measurement of the working electrode after CPC again revealed incorporation of nitrogen, but now also iron, on the surface. The detection of iron on the electrode surface by XPS raises the possibility that a heterogeneous iron catalyst may be responsible for (or contribute to) the electrocatalytic AO discussed above. Indeed, it is difficult, if not impossible, to reliably discount a contributing role for heterogenous (electro)catalysis.²¹ However, several lines of evidence lead us to suggest that a molecular, TPA-ligated iron catalyst dominates the aforementioned AO behavior. In the chronoamperogram for AO by the precatalyst [(TPA)Fe(MeCN)₂]OTf₂, no induction period was observed. Furthermore, a rinse test was performed with the BDD electrode following CPC using a fresh acetonitrile-ammonia solution. No catalytic current was passed in this case, ruling out a heterogeneous catalyst that is strongly attached to the electrode. Measurement of the catalyst solution after CPC with a clean BDD disk electrode

indicated a catalytic wave of similar intensity to that observed prior to CPC. To demonstrate the relative stability of the TPA-ligated Fe-species under catalytic conditions, 50 cycles of CV were performed, Figure 3.2A. Almost no reduction in catalytic current appeared between the first and last scan. While these experiments cannot reliably discount the possibility of a very rapidly formed, loosely bound and highly active heterogeneous catalyst forming under CPC experiments, we find such a scenario improbable.

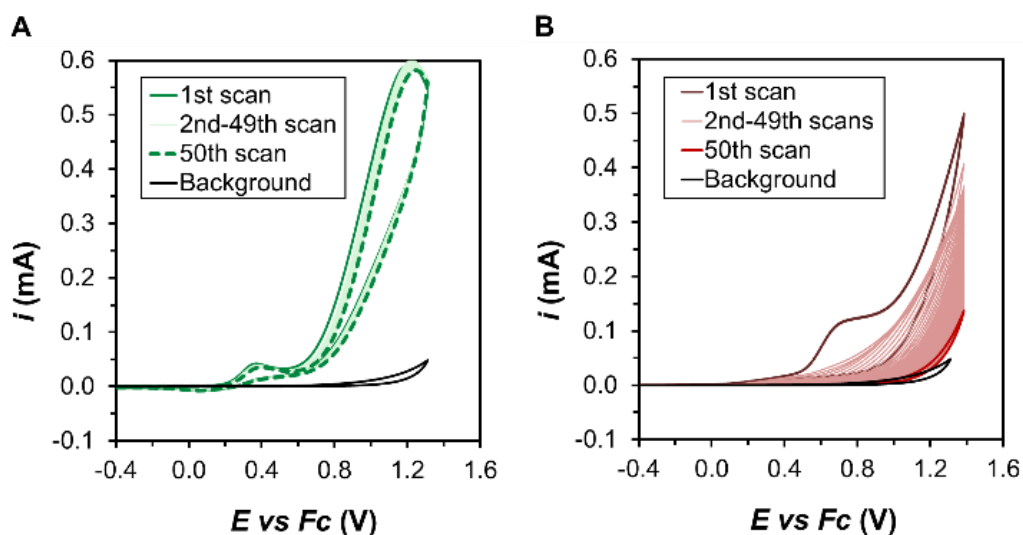


Figure 3.2. Cycling of (A) 2.5 mM [(TPA)Fe(MeCN)₂]OTf₂, or (B) 2.5 mM FeOTf₂, with a BDD disk electrode in an acetonitrile solution containing 50 mM NH₃ and 50 mM NH₄OTf. Pt wire was used as the counter electrode with a custom Ag/AgOTf reference electrode.

To probe this issue further, [(TPA)Fe(MeCN)₂]OTf₂ was replaced by FeOTf₂ as the precatalyst during CPC with ammonia. In this case, the current rapidly dropped to 10% of the initial current after only 1 h. After CPC, the XPS spectrum of the BDD electrode was almost identical to the spectrum obtained after CPC with [(TPA)Fe(MeCN)₂]OTf₂. 50 cycles of CV were also performed with FeOTf₂ in ammonia, Figure 3.2B. A continuous decrease in peak current, correlated with passivation of the electrode, was observed. In acetonitrile-ammonia solutions, we presume FeOTf₂ exists primarily as [Fe(NH₃)₆]OTf₂. The decrease

in current observed by CPC and CV, in addition to the iron observed on the electrode surface by XPS, establish the instability of $[\text{Fe}(\text{NH}_3)_6]\text{OTf}_2$ under the present conditions.

Given the instability of $[\text{Fe}(\text{NH}_3)_6]\text{OTf}_2$ under electrocatalytic conditions, we wondered if the source of the iron observed on the electrode surface post-CPC could be due to partial demetallation of TPA-ligated Fe species by NH_3 , thereby forming $\text{Fe}(\text{NH}_3)_6^{2+}$, which can then degrade at the BDD electrode. The speciation of $[(\text{TPA})\text{Fe}(\text{L})_2]\text{OTf}_2$ with varying ammonia concentrations was therefore studied by UV-vis spectroscopy (Figure 3.3A,B). A plot of absorbance at 400 nm vs $[\text{NH}_3]$, Figure 3.3A, displays three distinct regions of different slopes. We assign these as regions of equilibria corresponding to the

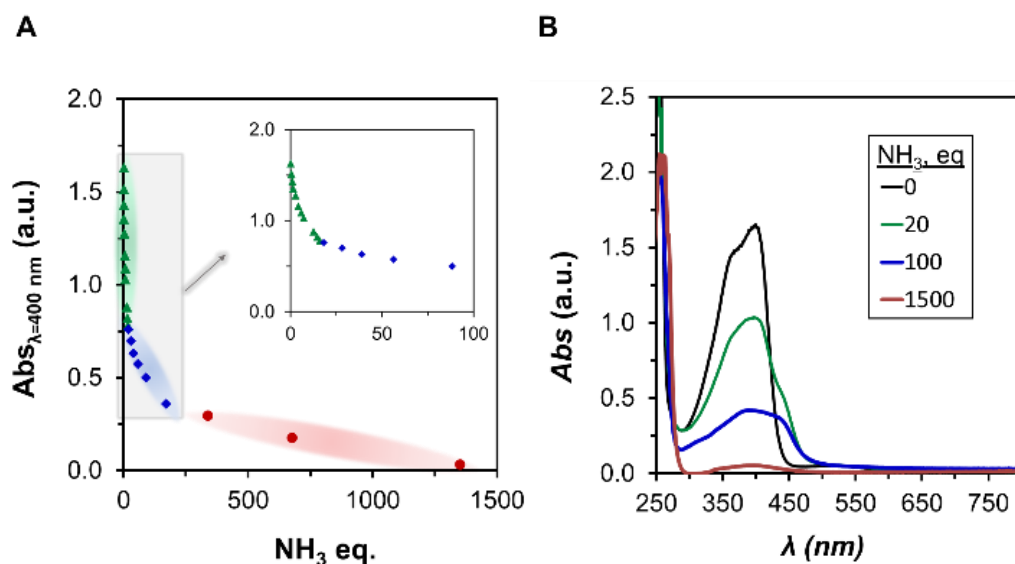


Figure 3.3. UV-vis monitoring of speciation. (A) Plot of absorbance at $\lambda_{\text{max}} = 400$ nm versus $[\text{NH}_3]$ demonstrating regions corresponding to mono-ammine, bis-ammine, and hexakis-ammine iron complexes. (B) UV-vis spectrum of 0.2 mM $[(\text{TPA})\text{Fe}(\text{MeCN})_2]\text{OTf}_2$ with 0, 20, 100, or 1500 eq NH_3 added in acetonitrile.

successive displacement by NH_3 of one MeCN (1–10 eq NH_3), a second MeCN (10–200 eq NH_3), and finally the additional displacement of TPA by NH_3 to form $\text{Fe}(\text{NH}_3)_6^{2+}$. In accord with these equilibria being reversible, the addition of free TPA to FeOTf_2 in MeCN with

excess NH_3 , to reproduce the electrocatalytic conditions, produces the E_1 and E_2 redox features as well as the UV-vis spectrum associated with $[(\text{TPA})\text{Fe}(\text{NH}_3)_2]^{2+}$; in the absence of FeOTf_2 , an irreversible oxidation wave for free TPA is instead observed at ~ 1.0 V. Consistent with the viability of $[(\text{TPA})\text{Fe}(\text{NH}_3)_2]\text{OTf}_2$, we were able to obtain its solid-state X-ray structure via crystals grown by diffusing NH_3 gas into a THF solution of dissolved $(\text{TPA})\text{FeOTf}_2$. The solid-state structure of $[(\text{TPA})\text{Fe}(\text{NH}_3)_2]\text{OTf}_2$ features four independent molecules in the asymmetric unit and interestingly, bond lengths that are consistent with the presence of *both* high- and low-spin iron centers (two of each type; see Figure 3.4 and SI).²² Given that $[(\text{TPA})\text{Fe}(\text{NH}_3)_2]\text{OTf}_2$ is structurally well-defined, as is $[(\text{TPA})\text{Fe}(\text{MeCN})_2]\text{OTf}_2$,¹⁸ an intermediate structure, $[(\text{TPA})\text{Fe}(\text{NH}_3)(\text{MeCN})]\text{OTf}_2$, is highly plausible and we presume the primary species present in the 1–10 eq NH_3 region.

Although the aforementioned electrocatalytic conditions include 130 eq NH_3 , a regime in which $[(\text{TPA})\text{Fe}(\text{NH}_3)_2]\text{OTf}_2$ dominates, there is likely a small population of $[\text{Fe}(\text{NH}_3)_6]^{2+}$ and also free TPA under these conditions. The source of iron on the electrode presumably results as $[\text{Fe}(\text{NH}_3)_6]^{2+}$ is continuously degraded, shifting the equilibrium toward further demetallation. Fortunately, degradation is slow, as evidenced by CV cycling experiments, the chronoamperogram as well as CVs and UV-vis acquired before and after CPC, (see SI).

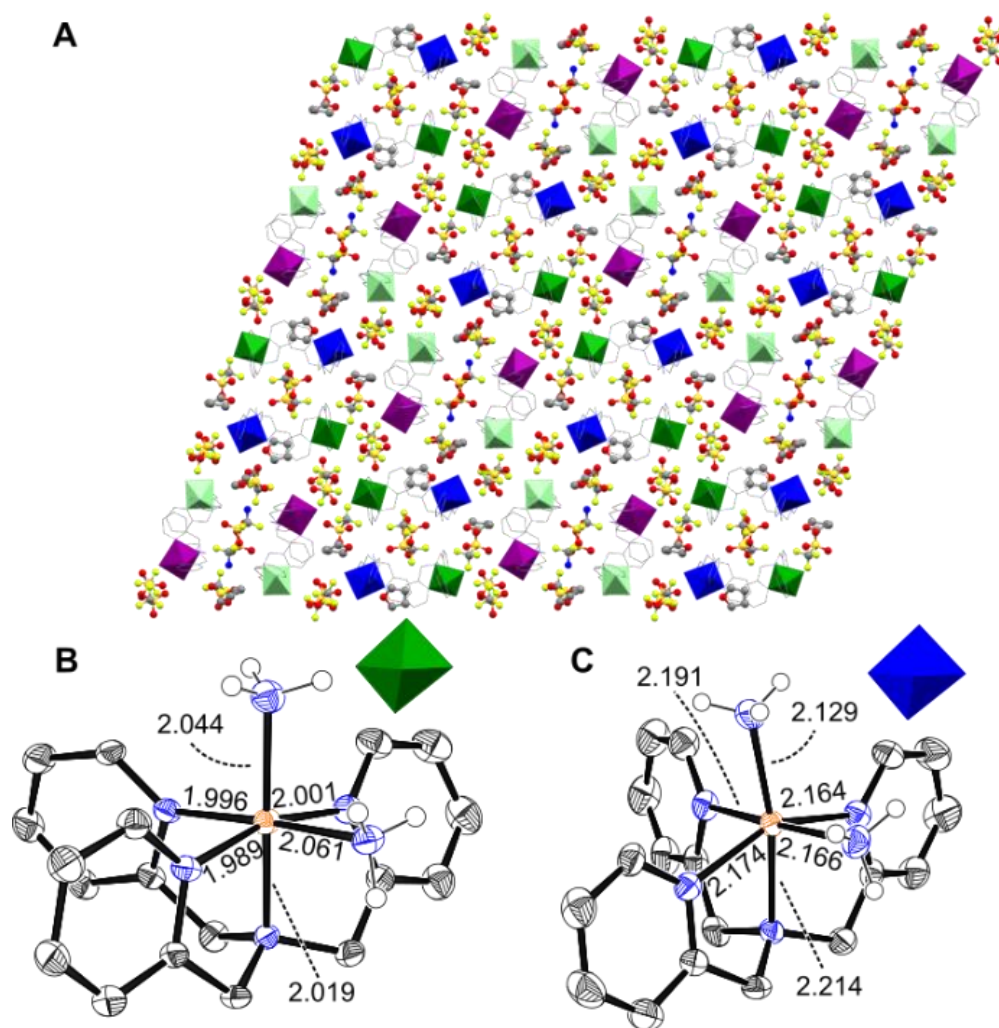
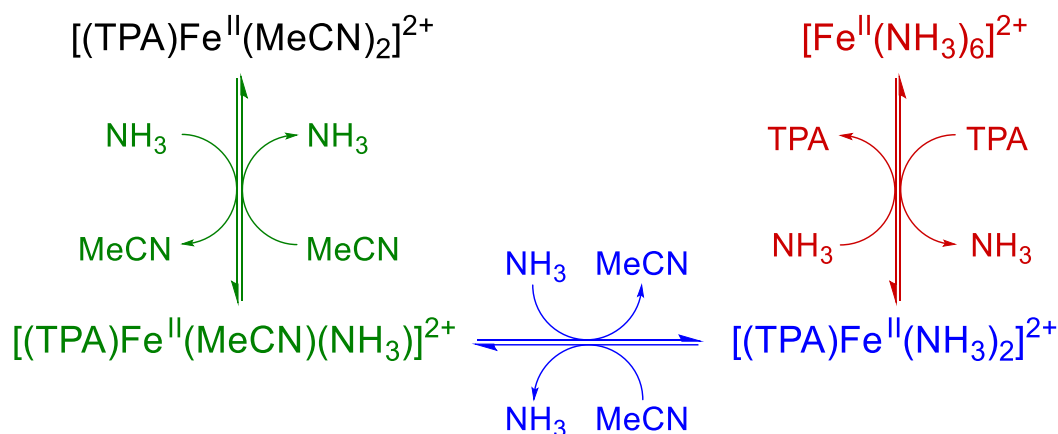


Figure 3.4. Solid-state crystal structure of $[(\text{TPA})\text{Fe}(\text{NH}_3)_2]\text{OTf}_2$ at 100 K. (A) View down the b -axis with 4 unit cells shown. Green/light green octahedra represent low spin Fe(II) sites, while blue/purple octahedra represent high spin Fe(II) sites. Representative low spin (B) and high spin (C) sites are shown, with bond lengths labeled in Å. Thermal ellipsoids are shown at 50% probability. Triflate counterions, hydrogen, and co-solvent are omitted for clarity.

3.2.3 Mechanistic insight into the first redox process (E_1). The sequential addition of NH_3 to $[(\text{TPA})\text{Fe}(\text{L})_2]^{2+}$ increased the catalytic current at E_2 (E_{cat}), Figure 3.1B. Another change observed in the cyclic voltammogram of $[(\text{TPA})\text{Fe}(\text{L})_2]^{2+}$ in MeCN with increasing amounts of ammonia is a shift in the potential of the first redox process, E_1 , toward more cathodic values. This observation indicates that the electron transfer step (E) in the oxidation is

coupled to a chemical step (C) involving NH_3 as a reactant. This EC mechanism is further supported by an increasing irreversibility at E_1 concomitant with the appearance of a new reduction peak E_1' at -0.4 V (Figure 3.5A), arising from the formation of a new species as $[\text{NH}_3]$ is increased.

Scheme 3.1. Equilibria relevant to substitution of acetonitrile and TPA by ammonia in acetonitrile solution for $[(\text{TPA})\text{Fe}(\text{L})_2]^{2+}$.



Interestingly, only one oxidation peak was observed at lower ammonia concentrations. This can be rationalized via a fast equilibrium between $[(\text{TPA})\text{Fe}(\text{MeCN})(\text{NH}_3)]^{2+}$ and $[(\text{TPA})\text{Fe}(\text{NH}_3)_2]^{2+}$ as described in Scheme 3.1. The bis-ammine complex is expected to have a more cathodically shifted oxidation potential (NH_3 being a stronger donor than MeCN). Thus, as the population of $[(\text{TPA})\text{Fe}(\text{NH}_3)_2]^{2+}$ is oxidized to $\text{Fe}(\text{III})$ near the electrode, the equilibrium shifts, driving coordination of a second NH_3 eq to $[(\text{TPA})\text{Fe}(\text{MeCN})(\text{NH}_3)]^{2+}$; the latter species should still be primarily in the $\text{Fe}(\text{II})$ oxidation state as it is expected to have a redox potential ~ 150 mV more positive than the $[(\text{TPA})\text{Fe}(\text{NH}_3)_2]^{2+}$.²³ Rapid solvent equilibration is expected for high spin iron(II), on the order of $\sim 10^4$ – 10^6 s^{-1} .²⁴

The voltammetric response of an EC mechanism is governed by the pseudo-first order equilibrium constant of the chemical step (K), as well as the competition between the pseudo-first order rate constant of the chemical step (k') and diffusion.^{25,26} Under our present conditions, the first redox event E_1 shows quasi-reversible character typical for the KE regime in the kinetic zone diagram, where the redox potential is governed by the following equation:

$$E_{ox} = E_{ox}^0 - \frac{RT}{F} \ln \left(\frac{k'_{1f}}{k'_{1b}} \right) \quad (\text{Equation 3.2})$$

F is the Faraday constant, R is the gas constant, T is the temperature, E_{ox} is the oxidation potential, E_{ox}^0 is the standard oxidation potential, and k'_{1f} and k'_{1b} are, respectively, the pseudo first order rate constants for the forward and backward chemical reaction. Using Equation 3.2, the change in peak potential with the natural logarithm of ammonia concentration reveals a linear dependence with a negative slope of -0.030 , in good agreement with the theoretical value of -0.026 (Figure 3.5B). Due to its character as a Brønsted base, one plausible explanation for the role of NH_3 in the chemical step following oxidation is the abstraction of a proton from one of the NH_3 ligands coordinated to Fe(III). Such a mechanism would produce NH_4^+ as a product, together with the oxidized iron complex $[(\text{TPA})\text{Fe}^{\text{III}}(\text{NH}_3)(\text{NH}_2)]^{2+}$. Accordingly, the E_1 potential with varying concentrations of NH_4^+ at a fixed concentration of NH_3 (Figure 3.5C) shows a linear relationship, with an observed slope of $+0.024$. This finding is in agreement with the predicted value of $+0.026$.

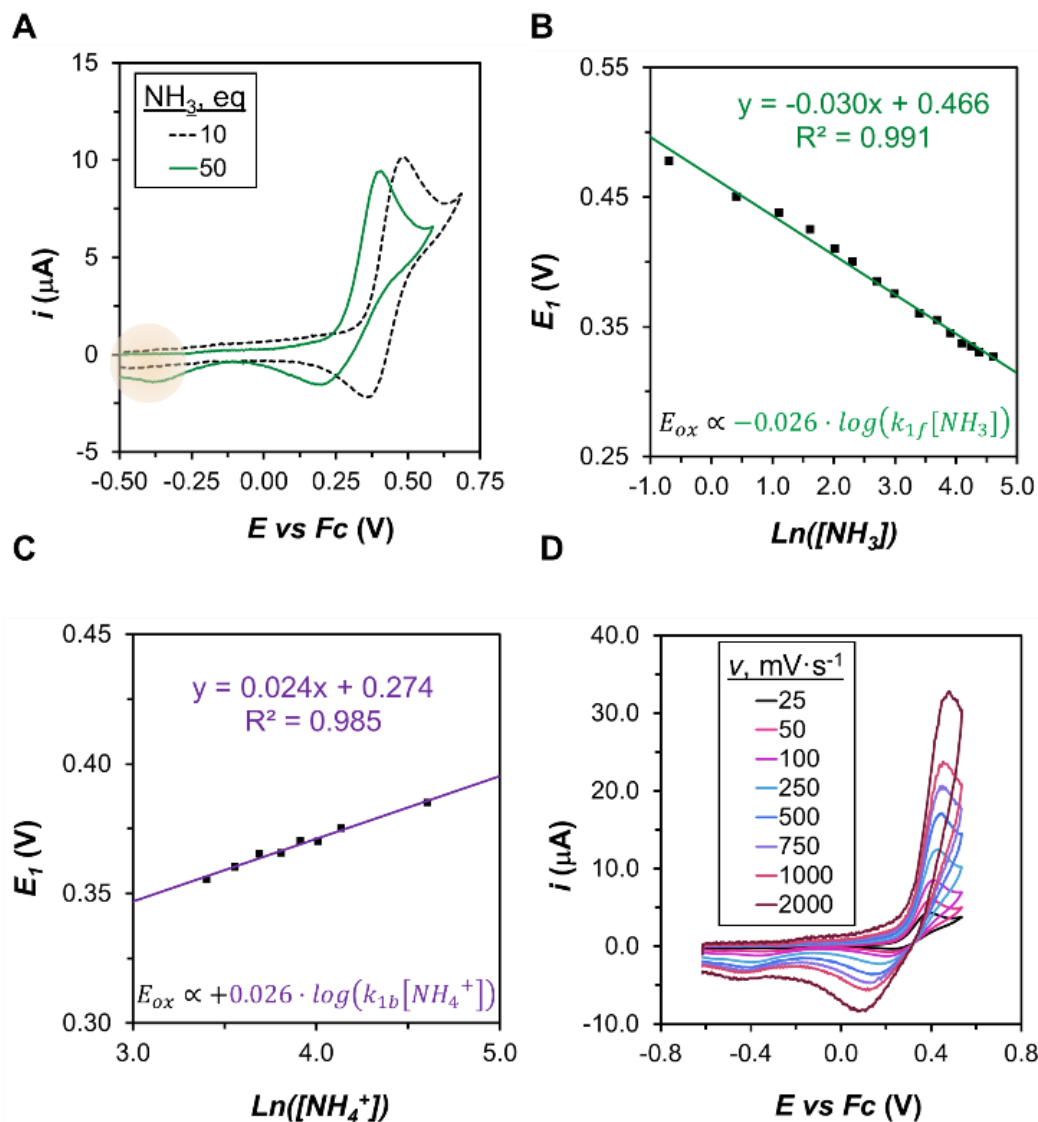
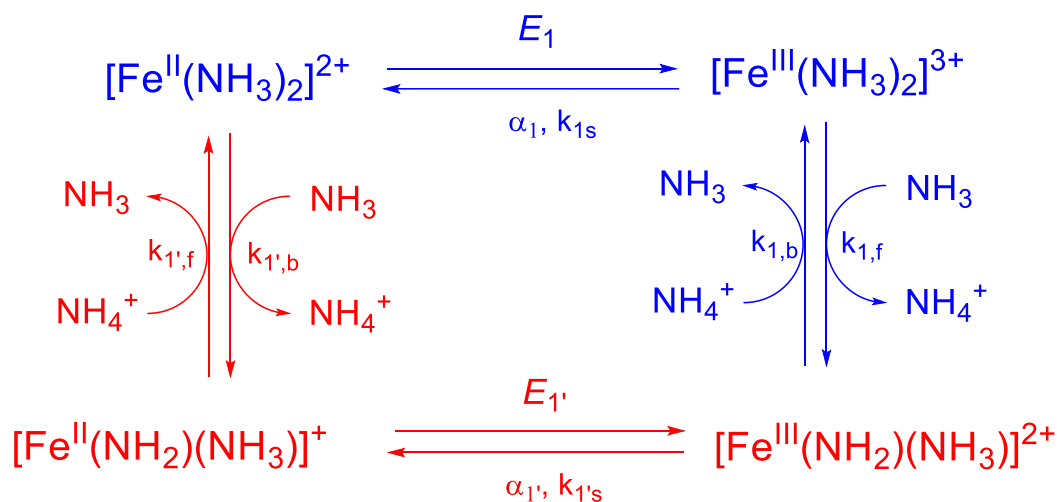


Figure 3.5. Evidence supporting an EC mechanism. (A) CV of an acetonitrile solution containing 0.5 mM $[(\text{TPA})\text{Fe}(\text{MeCN})_2]^{2+}$, 50 mM NH_4OTf , and 10 (black dashed trace) or 50 (solid green trace) eq NH_3 . (B) Plot of the potential for the first redox event E_1 versus the natural logarithm of $[\text{NH}_3]$. (C) Plot of the potential for the first redox event E_1 versus the natural logarithm of $[\text{NH}_4^+]$. (D) CV of an acetonitrile solution containing 0.5 mM of $[(\text{TPA})\text{Fe}(\text{MeCN})_2]^{2+}$, 50 mM NH_4OTf , and 50 mM NH_3 at different scan rates. CVs recorded with a BDD disk electrode, a Pt counter electrode, and a custom Ag/AgOTf reference electrode.

Hence, the proposed EC mechanism is consistent with the electrochemical behavior at E_1 as reactant, NH_3 , and product, NH_4^+ , concentrations are varied.

Using the above logic, we assign the reduction peak E_1 , appearing at -0.4 V in Figure 3.5A, to the one-electron reduction of $[(\text{TPA})\text{Fe}^{\text{III}}(\text{NH}_3)(\text{NH}_2)]^{2+}$. Upon its reduction, no return oxidation peak could be detected in the following anodic scan near -0.4 V, indicating fast protonation to regenerate $[(\text{TPA})\text{Fe}^{\text{II}}(\text{NH}_3)_2]^{2+}$. This is consistent with the basic character that might be expected for an octahedral Fe–NH₂ species.²⁷ Therefore, this first E_1 redox event involves a square mechanism, with a preliminary E_1C_1 oxidation reaction (blue equations in Scheme 3.2) coupled to a second E_2C_2 reduction reaction (red equations in Scheme 3.2).

Scheme 3.2. Proposed square mechanism for the first redox event, E_1 , at 0.4 V. The presence of the TPA ligand is implied for the species shown.



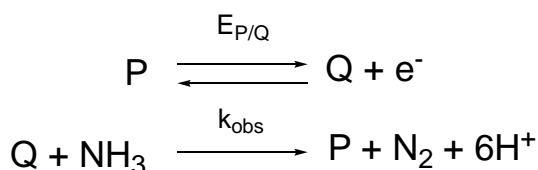
We have further confirmed this mechanism by performing cyclic voltammetry at different scan rates, as depicted in Figure 3.5D. At low scan rates, where C_1 reaches equilibrium, two reductive peaks could be detected with similar intensities, corresponding to $[(\text{TPA})\text{Fe}^{\text{III}}(\text{NH}_3)_2]^{3+}$ and $[(\text{TPA})\text{Fe}^{\text{III}}(\text{NH}_3)(\text{NH}_2)]^{2+}$. However, when the scan rate was increased, the reduction peak at around 0.2 V showed greater intensity as compared to the

peak at -0.4 V. This is a consequence of the relatively slow forward reaction, C_1 , as compared to the fast scan rate, such that C_1 does not reach equilibrium, and hence $[(\text{TPA})\text{Fe}^{\text{III}}(\text{NH}_3)_2]^{2+}$ is the main species reduced at the electrode.

Analysis of the peak currents at E_1 obtained from CVs at different scan rates reveals a linear relationship with $\nu^{1/2}$, following the predicted behavior from the Randles-Sevcik equation for an electrochemically reversible electron transfer process of a freely diffusing molecule in solution.²⁸ Further analysis of the current corresponding to the oxidative peak with increasing concentrations of $[(\text{TPA})\text{Fe}(\text{L})_2]^{2+}$ again reveals the linear dependence expected for a one electron oxidation. This data, in combination with the well-behaved shift in E_1 potential with both NH_3 and NH_4^+ concentration, collectively support a primary process at E_1 to form a reactive $\text{Fe}^{\text{III}}\text{-NH}_2$ species.

3.2.4 Mechanistic insight into the catalytic process (E_2). We performed a similar analysis of the E_2 (E_{cat}) event where fast catalysis is observed. While a detailed analysis for this six-electron/six-proton process can in principle be performed,²⁹ in practice such an analysis quickly becomes intractable. A common mechanistic approximation is therefore to consider the simplest case scenario, where electron transfer from the catalyst to the electrode is

Scheme 3.3. A simplified catalytic mechanism for ammonia oxidation at $E_2 \approx 1.1$ V. P and Q represent the inferred intermediates $[(\text{TPA})\text{Fe}^{\text{III}}(\text{NH}_3)(\text{NH}_2)]^{2+}$ and its one-electron oxidized species $[\text{Fe}^{\text{IV}}(\text{NH}_3)(\text{NH}_2)]^{3+}$, respectively. The latter intermediate would then react with ammonia in a process that ultimately releases N_2 . $E_{\text{P/Q}}$ is the potential for the P/Q redox couple, and k_{obs} is the apparent second-order rate constant of the catalytic chemical step.



followed by a rate determining homogeneous catalytic reaction with the substrate, EC_{cat} , as shown in Scheme 3.3.^{25,30}

A related strategy has been previously applied to electrocatalytic redox processes for CO_2 reduction³¹ and water oxidation,³² and provides essential information regarding the mechanism and the overall kinetics for the catalytic process. Such an approach is justified here because the potential of the first EC step (E_1) is cathodically well separated from E_2 . Furthermore, oxidation following an N–N bond formation step is expected to occur at less oxidizing potentials. In support of this notion, we found that a CV of $[(TPA)Fe(L)_2]^{2+}$ in acetonitrile with added hydrazine displayed a catalytic oxidation around 0.4 V. Our primary assumption is thus that electrocatalytic NH_3 oxidation to N_2 is triggered via a single electron transfer step that occurs at a substantially more oxidizing potential than all other steps. If correct, simplification to an EC mechanism is reasonable, and it then becomes possible to obtain a kinetic constant (k_{obs}) that reflects the overall rate of the catalytic reaction, after scaling for the number of electrons transferred (n).³³

To calculate k_{obs} , we performed a foot of the wave analysis (FOWA).³¹ Due to non-Nernstian behavior in the ET step (see Supporting Information for further details), the Butler-Volmer law, which includes a charge transfer coefficient (α) and the rate constant for interfacial electron transfer (k_s), was utilized:³⁴

$$FIT(E_{cat}^0 - E) = \frac{\frac{i}{i_p}}{1 - 0.446 \frac{i}{i_p} \frac{\sqrt{D_{cat}}}{k_s} \sqrt{\frac{F}{R \cdot T}} \nu \exp \left[\alpha \frac{F}{R \cdot T} (E_{cat}^0 - E) \right]} = \frac{n \cdot 2.24 \cdot \sqrt{\frac{R \cdot T}{F \cdot \nu}} \cdot k'_{obs}}{1 + \exp \left[\frac{F}{R \cdot T} (E_{cat}^0 - E) \right]} \quad (\text{Equation 3.3})$$

Plotting the FIT equation versus $1/(1+\exp[F/(RT)(E_{\text{cat}}-E])$ gives the value for pseudo first-order constant $k'_{\text{obs}}=k_{\text{obs}} \cdot [\text{NH}_3]$ (see SI). To use these equations, α and k_s were determined from the precatalytic wave by analyzing the peak potential at different scan rates (see SI).²⁵ We found an α value of 0.66, close to the typical value when use of the Butler-Volmer equation is necessary,²⁵ and a diffusion coefficient D_{cat} : $9.5 \cdot 10^{-10}$ ($\text{m}^2 \cdot \text{s}^{-1}$), which is typical for molecular complexes in solution (see Supporting Information).³⁵ With these values, we could obtain the kinetic constant for the electron transfer k_s of around $111 \text{ m} \cdot \text{s}^{-1}$. These data enable a FOWA according to Equation 3.3, which provides a second order apparent rate constant, k_{obs} , of $3.7 \cdot 10^7 \text{ M}^{-1} \cdot \text{s}^{-1}$ on average for different concentrations of catalyst (Figure 3.6A; see SI for details). Hence, this iron catalyst for AO is able to operate at a remarkably fast rate under a large applied bias of 1.1 V.

In addition to providing kinetic information, this method of analysis also offers important mechanistic information about the catalytic process, because the validity of these equations is intrinsically related to the validity of the assumed mechanism. Our assumed mechanism includes a rate-determining step which is first order both in catalyst and in NH_3 . Accordingly, the calculated pseudo-first order rate constant, k'_{obs} , should be constant with respect to the $[(\text{TPA})\text{Fe}(\text{L})_2]^{2+}$ concentration (because k'_{obs} is normalized by its molarity), and should respond linearly to the NH_3 concentration. We have confirmed both relationships by analysis at different concentrations of $[(\text{TPA})\text{Fe}(\text{L})_2]^{2+}$ and $[\text{NH}_3]$ (Figure 3.6A,B).

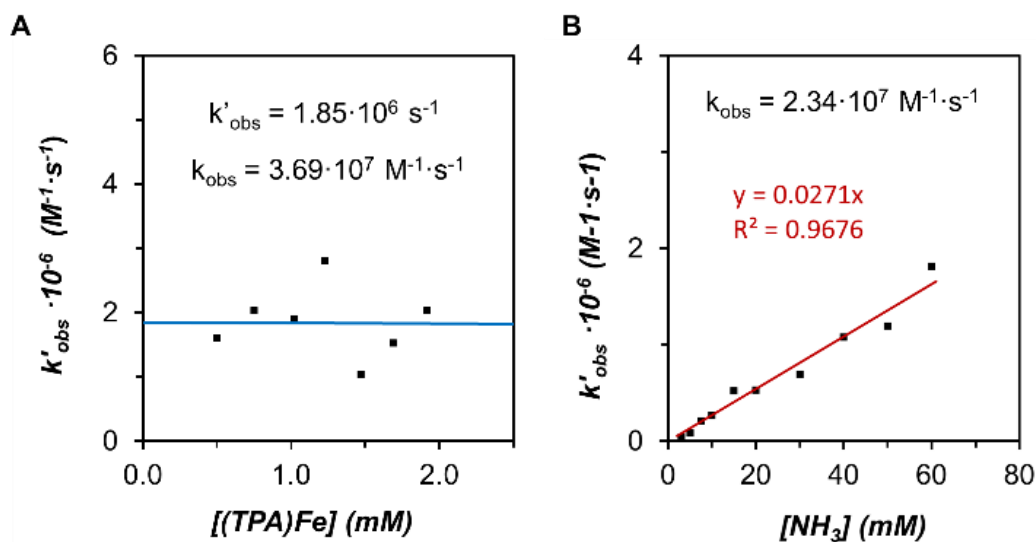


Figure 3.6. Rate law data. (A) Dependence of the calculated k'_{obs} on the concentration of $[(\text{TPA})\text{Fe}(\text{MeCN})_2]^{2+}$ precatalyst. (B) Dependence of the calculated k'_{obs} on the concentration of NH_3 . In both cases, k'_{obs} has been calculated using FOWA as described in the SI.

3.3 Conclusion

With interest growing in the study of molecular (electro)catalysts for AO, a fascinating multi-electron redox reaction that represents the microscopic reverse of N_2 -to- NH_3 conversion, electrochemically well-defined model systems are needed. In this context we have described in detail the capacity of a polypyridyl iron catalyst, $[(\text{TPA})\text{Fe}(\text{MeCN})_2]\text{OTf}_2$, to perform AO at extremely fast rates ($\sim 10^7 \text{ M}^{-1}\cdot\text{s}^{-1}$ via FOWA) under the application of a 1.1 V applied bias. We have also used CPC to confirm that N_2 is selectively formed via this AO reaction, confirming as many as 16 eq of N_2 (32 eq NH_3 being consumed) per Fe. While TONs do not necessarily reflect overall efficiency of a catalyst, the value we measure is higher than other values reported to date. Mechanistic data extracted from a range of electrochemical studies suggest that an $\text{Fe}^{\text{III}}\text{-NH}_2$ species is generated at the first E_1 process (0.4 V vs Fc/Fc^+) via net H-atom removal from intermediate $[(\text{TPA})\text{Fe}(\text{NH}_3)_2]^{2+}$.

The first wave, E_1 at ~ 0.4 V vs Fc/Fc⁺, has been determined to correspond to a subsequent electron and proton transfer (EC) from a newly characterized [(TPA)Fe(NH₃)₂]²⁺ species to generate a reactive terminal amide [(TPA)Fe^{III}(NH₂)(NH₃)]²⁺ intermediate. This intermediate then undergoes a subsequent EC step at E_2 around 1.1 V, and this is the feature associated with catalytic AO. We speculate that at this potential Fe(III) is oxidized to Fe(IV), possibly via an [(TPA)Fe^{IV}(NH₃)(NH₂)]³⁺ intermediate. Future studies will focus on the direct spectroscopic detection of these (or other) candidate intermediates. Regardless, we intuit that N–N bond forming steps occur subsequent to the generation of [(TPA)Fe^{IV}(NH₃)(NH₂)]³⁺ or some similar species. We cannot yet determine from the available data whether or not such steps are intramolecular (e.g., via N–N coupling from adjacent Fe–NH_x ligands) or intermolecular (e.g., via nucleophilic attack of NH₃ on Fe–NH_x). We are, however, able to say from FOWA that the overall catalytic reaction is first order in both [(TPA)Fe(L)₂]²⁺ and NH₃.

The catalysis is ultimately arrested due to passivation of the BDD working electrode surface, likely via a combination of incorporation of nitrogen and iron, which can be detected via analysis of the electrode post CPC. It may be that exploring less labile polydentate ligands, such as those possessing a negative charge, will attenuate the lability of TPA that is operative in this system and ultimately leads to catalyst degradation. Such approaches may also afford a catalyst that operates at less oxidizing potentials, though this may in turn attenuate the overall catalytic rate.

3.4 References

- ¹ (a) Service, R. F. Ammonia—A Renewable Fuel Made from Sun, Air, and Water—Could Power the Globe without Carbon. *Science* **2018**, aau8489 DOI:10.1126/science.aau7489. (b) Wan, Y.; Xu, J.; Ly, R. Heterogeneous Electrocatalysts Design for Nitrogen Reduction Reaction Under Ambient Conditions. *Mater. Today* **2019**, *27*, 69–90. (c) Martin, A. J.; Shinagawa, T.; Perez–Ramirez, J. Electrocatalytic Reduction of Nitrogen: From Haber–Bosch to Ammonia Artificial Leaf. *Chem* **2019**, *5*, 263–283. (d) Cui, X.; Tang, C.; Zhang, Q. A Review of Electrocatalytic Reduction of Dinitrogen to Ammonia Under Ambient Conditions. *Adv. Energy Mater.* **2018**, *8*, 1800369. (e) Valera-Medina, A.; Xiao, H.; Owen-Jones, M.; David, W. I. F.; Bowen, P. J. Ammonia for Power. *Prog. Energy Combust. Sci.* **2018**, *69*, 63–102. (f) Adli, N. M.; Zhang, H.; Mukherjee, S.; Wu, G. Ammonia Oxidation Electrocatalysis for Hydrogen Generation and Fuel Cells. *J. Electrochem. Soc.* **2018**, *165*, J3130–J3147.
- ² (a) Cairns, E. J.; Simons, E. L.; Tevebaugh, A. D. Ammonia–Oxygen Fuel Cell. *Nature* **1968**, *217*, 780–781. (b) Lan, R.; Tao, S. Ammonia as a Suitable Fuel for Fuel Cells. *Front. in Energy Res.* **2014**, *2*, 00035. (c) Zhong, C.; Hu, W. B.; Cheng, Y. F. Recent Advances in Electrocatalysts for Electro-Oxidation of Ammonia. *J. Mater. Chem. A*, **2013**, *1*, 3216–3238. (d) Gang, L.; van Grondelle, J.; Anderson, B. G.; van Santen, R. A. Selective Low Temperature NH₃ Oxidation to N₂ on Copper-Based Catalysts. *J. Catal.* **1999**, *186*, 100–109. (e) Cui, X.; Chen, L.; Wang, Y.; Chen, H.; Zhao, W.; Li, Y.; Shi, J. Fabrication of Hierarchically Porous RuO₂–CuOAl–ZrO₂ Composite as Highly Efficient Catalyst for Ammonia-Selective Catalytic Oxidation. *ACS Catal.* **2014**, *4*, 2195–2206. (f) Song, S.; Jiang, S. Selective Catalytic Oxidation of Ammonia to Nitrogen over CuO/CNTs: The Promoting Effect of the Defects of CNTs on the Catalytic Activity and Selectivity. *Appl. Catal. B* **2012**, *117–118*, 346–350. (g) Katsounaros, I.; Chen, T.; Gewirth, A. A.; Markovic, N. M.; Koper, M. T. M. Evidence for Decoupled Electron and Proton Transfer in the Electrochemical Oxidation of Ammonia on Pt(100). *J. Phys. Chem. Lett.* **2016**, *7*, 387–392.
- ³ (a) Staffell, I.; Scamman, D.; Abad, A. V.; Balcombe, P.; Dodds, P. E.; Ekins, P.; Shah, N.; Ward, K. R. The Role of Hydrogen and Fuel Cells in the Global Energy System. *Energy Environ. Sci.* **2019**, *12*, 463–491. (b) Joghee, P.; Malik, J.; Pylypenko, S.; O’Hayre, R. A Review on Direct Methanol Fuel Cells – In the Perspective of Energy and Sustainability. *MRS Energy & Sustainability*, **2015**, *2*, E3.
- ⁴ (a) Stucke, N.; Flöser, B. M.; Wyrich, T.; Tuczek, F. Nitrogen Fixation Catalyzed by Transition Metal Complexes: Recent Developments. *Eur. J. Inorg. Chem.* **2018**, 1337–1355. (b) Nishibayashi, Y. Development of Catalytic Nitrogen Fixation Using Transition Metal–Dinitrogen Complexes Under Mild Reaction Conditions. *Dalton Trans.* **2018**, *47*, 11290–11297.
- ⁵ (a) Yandulov, D. V.; Schrock, R. R. Catalytic Reduction of Dinitrogen to Ammonia at a Single Molybdenum Center. *Science*, **2003**, *301*, 76–78. (b) Anderson, J. S.; Rittle, J.; Peters, J. C. Catalytic Conversion of Nitrogen to Ammonia by an Iron Model Complex. *Nature*, **2013**, *501*, 84–87. (c) Arashiba, K.; Miyake, Y.; Nishibayashi, Y. A Molybdenum Complex Bearing PNP-type Pincer Ligands Leads to the Catalytic Reduction of Dinitrogen into Ammonia. *Nat. Chem.* **2011**, *3*, 120–125. (d) Chalkley, M. J.; Castillo, T. J. Del; Matson, B. D.; Peters, J. C. Fe-Mediated Nitrogen Fixation with a Metallocene Mediator: Exploring pK_a Effects and Demonstrating Electrocatalysis. *J. Am. Chem. Soc.* **2018**, *140*, 6122–6129. (e) Ashida, Y.; Arashiba, K.; Nakajima, K.; Nishibayashi, Y. Molybdenum-catalyzed Ammonia Production with Samarium Diiodide and Alcohols or Water. *Nature* **2019**, *568*, 536–540.
- ⁶ Minteer, S. D.; Christopher, P.; Linic, S. Recent Developments in Nitrogen Reduction Catalysts: A Virtual Issue. *ACS Energy Lett.* **2019**, *4*, 1163–166.

- ⁷ (a) Lancaster, K. M.; Caranto, J. D.; Majer, S. H.; Smith, M. A. Alternative Bioenergy: Updates to and Challenges in Nitrification Metalloenzymology. *Joule*, **2018**, *3*, 421–441. (b) Kartal, B.; Keltjens, J. T. Anammox Biochemistry: a Tale of Heme c Proteins. *Trends Biochem. Sci.* **2016**, *41*, 998–1011.
- ⁸ Warren, J. J.; Tronic, T. A.; Mayer, J. M. Thermochemistry of Proton-Coupled Electron Transfer Reagents and its Implications. *Chem. Rev.* **2010**, *110*, 6961–7001.
- ⁹ Buhr, J. D.; Taube, H. Oxidation of $[\text{Os}(\text{NH}_3)_5\text{CO}]^{2+}$ to $[(\text{Os}(\text{NH}_3)_4\text{CO})_2\text{N}_2]^{4+}$. *Inorg. Chem.* **1979**, *18*, 2208–2212.
- ¹⁰ Thompson, M. S.; Meyer, T. J. Oxidation of Coordinated Ammonia to Nitrate. *J. Am. Chem. Soc.* **1981**, *103*, 5577–5579.
- ¹¹ (a) Ishitani, O.; White, P. S.; Meyer, T.J. Formation of Dinitrogen by Oxidation of $[(\text{bpy})_2(\text{NH}_3)\text{RuORu}(\text{NH}_3)(\text{bpy})_2]^{4+}$. *Inorg. Chem.* **1996**, *35*, 2167–2168. (b) Ishitani, O.; Ando, E.; Meyer, T. J. Dinitrogen Formation by Oxidative Intramolecular N–N Coupling in *cis,cis*- $[(\text{bpy})_2(\text{NH}_3)\text{RuORu}(\text{NH}_3)(\text{bpy})_2]^{4+}$. *Inorg. Chem.* **2003**, *42*, 1707–1710.
- ¹² Collman, J. P.; Hutchison, J. E.; Ennis, M. S.; Lopez, M. A.; Guilard, R. Reduced Nitrogen Hydride Complexes of a Cofacial Metallodiporphyrin and Their Oxidative Interconversion. An Analysis of Ammonia Oxidation and Prospects for a Dinitrogen Electroreduction Catalyst Based on Cofacial Metallodiporphyrins. *J. Am. Chem. Soc.* **1992**, *114*, 8074–8080.
- ¹³ Habibzadeh, F.; Miller, S. L.; Hamann, T. W.; Smith, M. R. Homogeneous Electrocatalytic Oxidation of Ammonia to N_2 Under Mild Conditions. *Proc. Natl. Acad. Sci. U.S.A.* **2019**, *116*, 2849–2853.
- ¹⁴ (a) Man, W.; Tang, T.; Wong, T.; Lau, T.; Peng, S.; Wong, W. Highly Electrophilic (Salen)ruthenium(VI) Nitrido Complexes. *J. Am. Chem. Soc.* **2004**, *126*, 478–479. (b) Scheibel, M. G.; Wu, Y.; Stückl, A. C.; Krause, L.; Carl, E.; Stalke, D.; de Bruin, B.; Schneider, S. Synthesis and Reactivity of a Transient, Terminal Nitrido Complex of Rhodium. *J. Am. Chem. Soc.* **2013**, *135*, 17719–17722. (c) Scheibel, M. G.; Abbenseth, J.; Kinauer, M.; Heinemann, F. W.; Würtele, C.; de Bruin, B.; Schneider, S. Homolytic N–H Activation of Ammonia: Hydrogen Transfer of Parent Iridium Ammine, Amide, Imide, and Nitride Species. *Inorg. Chem.* **2015**, *54*, 9290–9302. (d) Abbenseth, J.; Finger, M.; Würtele, C.; Kananmascheff, M.; Schneider, S. Coupling of Terminal Iridium Nitrido Complexes. *Inorg. Chem. Front.* **2016**, *3*, 469–477. (e) Clarke, R. M.; Storr, T. Tuning Electronic Structure To Control Manganese Nitride Activation. *J. Am. Chem. Soc.* **2016**, *138*, 15299–15302. (f) Bezdek, M. J.; Guo, S.; Chirik, P. J. Coordination-Induced Weakening of Ammonia, Water, and Hydrazine X–H Bonds in a Molybdenum Complex. *Science*, **2016**, *354*, 730–733. (g) Bhattacharya, P.; Heiden, Z. M.; Wiedner, E. S.; Rauegi, S.; Piro, N. A.; Kassel, W. S.; Bullock, R. M.; Mock, M. T. Ammonia Oxidation by Abstraction of Three Hydrogen Atoms from a Mo– NH_3 Complex. *J. Am. Chem. Soc.* **2017**, *139*, 2916–2919. (h) Keener, M.; Peterson, M.; Hernández Sánchez, R.; Oswald, V. F.; Wu, G.; Ménard, G. Towards Catalytic Ammonia Oxidation to Dinitrogen: A Synthetic Cycle by Using a Simple Manganese Complex. *Chem. Eur. J.* **2017**, *23*, 11479–11484.
- ¹⁵ Bhattacharya, P.; Heiden, Z. M.; Chambers, G. M.; Johnson, S. I.; Bullock, R. M.; Mock, M. T. Catalytic Ammonia Oxidation to Dinitrogen by Hydrogen Atom Abstraction. *Angew. Chem. Int. Ed.* **2019**, *58*, 11618–11624.
- ¹⁶ Nakajima, K.; Toda, H.; Sakata, K.; Nishibayashi, Y. Ruthenium-Catalysed Oxidative Conversion of Ammonia into Dinitrogen. *Nat. Chem.* **2019**, *11*, 702–709.
- ¹⁷ For select examples see: (a) Fillol, J. L.; Codolà, Z.; Garcia-Bosch, I.; Gómez, L.; Pla, J. J.; Costas, M. Efficient Water Oxidation Catalysts Based on Readily Available Iron Coordination Complexes. *Nat. Chem.* **2011**, *3*, 807–813. (b) Zhang, B.; Li, F.; Yu, F.; Cui, H.; Zhou, X.; Li, H.; Wang, Y.; Sun, L. Homogeneous Oxidation of Water by Iron

- Complexes with Macrocyclic Ligands. *Chem. Asian J.* **2014**, *9*, 1515–1518. (c) To, W.-P.; Chow, T. W.-S.; Tse, C.-W.; Guan, X.; Huang, J.-S.; Che, C.-M. Water Oxidation Catalysed by Iron Complex of N,N'-dimethyl-2,11-diaza[3,3](2,6)pyridinophane. Spectroscopy of Iron–Oxo Intermediates and Density Functional Theory Calculations. *Chem. Sci.* **2015**, *6*, 5891–5903. (d) Das, B.; Orthaber, A.; Ott, S.; Thapper, A. Iron Pentapyridyl Complexes as Molecular Water Oxidation Catalysts: Strong Influence of a Chloride Ligand and pH in Altering the Mechanism. *ChemSusChem* **2016**, *9*, 1178–1186. (e) Coggins, M. K.; Zhang, M.-T.; Vannucci, A. K.; Dares, C. J.; Meyer, T. J. Electrocatalytic Water Oxidation by a Monomeric Amidate-Ligated Fe(III)-Aqua Complex. *J. Am. Chem. Soc.* **2014**, *136*, 5531–5534. (f) Wickramasinghe, L. D.; Zhou, R.; Zong, R.; Vo, P.; Gagnon, K.J.; Thummel, R. P. Iron Complexes of Square Planar Tetradentate Polypyridyl-Type Ligands as Catalysts for Water Oxidation. *J. Am. Chem. Soc.* **2015**, *137*, 13260–13263.
- ¹⁸ Diebold, A.; Hagen, K. S. Iron(II) Polyamine Chemistry: Variation of Spin State and Coordination Number in Solid State and Solution with Iron(II) Tris(2-pyridylmethyl)amine Complexes. *Inorg. Chem.* **1998**, *37*, 215–223.
- ¹⁹ Charge passed and Faradaic efficiencies are averaged over six experiments. Turn over numbers are averaged over two experiments with 2.5 mmol [(TPA)Fe(MeCN)₂]OTf₂, the optimum condition studied. Reported values for N₂ are all corrected for background nitrogen, determined by integrating the oxygen peak in the gas chromatograms. For N₂ produced by 2.5 mmol [(TPA)Fe(L)₂]²⁺, 1.0 equivalent of background N₂ produced by the electrode has been subtracted.
- ²⁰ Lee, K. J.; McCarthy, B. D.; Dempsey, J. L. On Decomposition, Degradation, and Voltammetric Deviation: The Electrochemist's Field Guide to Identifying Precatalyst Transformation. *Chem. Soc. Rev.* **2019**, *48*, 2927–2945.
- ²¹ Folkman, S. J.; Soriano-Lopez, J.; Galán-Mascarós, J.; Finke, R. J. Electrochemically Driven Water-Oxidation Catalysis Beginning with Six Exemplary Cobalt Polyoxometalates: Is It Molecular, Homogeneous Catalysis or Electrode-Bound, Heterogeneous CoO_x Catalysis? *J. Am. Chem. Soc.*; **2018**, *140*, 12040–12055.
- ²² Solid-State structures simultaneously featuring metal centers in different spin states are uncommon but not unprecedented. See, for example: (a) Sheu, C.; Pillet, S.; Lin, Y.; Chen, S.; Hsu, I.; Lecomte, C.; Wang, Y. Magnetostructural Relationship in the Spin-Crossover Complex t-{Fe(abpt)₂[N(CN)₂]₂}: Polymorphism and Disorder Phenomenon. *Inorg. Chem.* **2008**, *47*, 10866–10874. (b) Sheu, C.; Chen, S.; Wang, S.; Lee, G.; Liu, Y.; Wang, Y. The Commensurate Modulated Structure of the Metastable State in Spin Crossover Complex [Fe(abpt)₂(NCS)₂]. *Chem. Commun.* **2009**, 7512–7514.
- ²³ The bis-ammine has a redox potential 300 mV lower than the bis-acetonitrile complex, therefore replacement of each MeCN by NH₃ can be estimated to shift the potential by 150 mV assuming a linear relationship.
- ²⁴ Funahashi, S.; Jordan, R. B. Solvent-Exchange Kinetics in Iron(II) Solutions of N,N-Dimethylformamide and Dimethyl Sulfoxide Studied by Nuclear Magnetic Resonance Line Broadening. *Inorg. Chem.* **1977**, *16*, 1301–1306.
- ²⁵ Costentin, C.; Savéant, J. M. *Elements of Molecular and Biomolecular Electrochemistry: An Electrochemical Approach to Electron Transfer Chemistry*, 2nd ed.; John Wiley & Sons, Hoboken, NJ, 2006.
- ²⁶ Savéant, J.-M.; Vianello, E. Potential-Sweep Voltammetry: General Theory of Chemical Polarization. *Electrochim. Acta*, **1967**, *12*, 629–646.
- ²⁷ Fox, D. J.; Bergman, R. G. Synthesis of a First-Row Transition Metal Parent Amido Complex and Carbon Monoxide Insertion into the Amide N-H Bond. *J. Am. Chem. Soc.* **2003**, *125*, 8984–8985.

- ²⁸ Bard, A. J.; Faulkner, L. R. *Electrochemical Methods: Fundamentals and Applications*, 2nd ed.; John Wiley & Sons, Hoboken, NJ, 2001.
- ²⁹ Costentin, C.; Savéant, J.-M. Multielectron, Multistep Molecular Catalysis of Electrochemical Reactions: Benchmarking of Homogeneous Catalysts. *ChemElectroChem*, **2014**, *1*, 1226–1236.
- ³⁰ Andrieux, C. P.; Blocman, C.; Dumas-Bouchiat, J. M.; M'Halla, F.; Savéant, J. M. Homogeneous Redox Catalysis of Electrochemical Reactions: Part V. Cyclic Voltammetry. *J. Electroanal. Chem.* **1980**, *113*, 19–40
- ³¹ Costentin, C.; Drouet, S.; Robert, M.; Savéant, J.-M. Turnover Numbers, Turnover Frequencies, and Overpotential in Molecular Catalysis of Electrochemical Reactions. Cyclic Voltammetry and Preparative-Scale Electrolysis. *J. Am. Chem. Soc.* **2012**, *134*, 11235–11242.
- ³² Matheu, R.; Neudeck, S.; Meyer, F.; Sala, X.; Llobet, A. Foot of the Wave Analysis for Mechanistic Elucidation and Benchmarking Applications in Molecular Water Oxidation Catalysis. *ChemSusChem*. **2016**, *9*, 3361–3369.
- ³³ Wang, V. C.-C.; Johnson, B. A. Interpreting the Electrocatalytic Voltammetry of Homogeneous Catalysts by the Foot of the Wave Analysis and Its Wider Implications. *ACS Catal.* **2019**, *9*, 7109–7123.
- ³⁴ Costentin, C.; Drouet, S.; Robert, M.; Savéant, J.-M. A Local Proton Source Enhances CO₂ Electroreduction to CO by a Molecular Fe Catalyst. *Science*, **2012**, *338*, 90–94.
- ³⁵ Baur, J. E.; Diffusion Coefficients. In *Handbook of Electrochemistry*. Zoski, C. G.; Elsevier, 2007, 829–848.